Journal of Materials Chemistry A

PAPER

Cation disorder and phase transitions in the structurally complex solar cell material Cu_2ZnSnS_4

Received 26th April 2017
Accepted 18th July 2017

www.rsc.org

C.J. Bosson[a], M.T. Birch[a], D.P. Halliday[a*], K.S. Knight[b,c], A.S. Gibbs[d], and P.D. Hatton[a]

Cu_2ZnSnS_4 (CZTS) is a technologically important and complex quaternary semiconductor and a highly promising material for the absorber layer in sustainable thin film solar cells. Its photovoltaic performance is currently limited by low open-circuit voltage, thought to be due to a range of point defects such as disorder between the copper and zinc lattice sites. This is the highest-resolution neutron diffraction study reported for CZTS, which unambiguously identifies the crystal symmetry and accurately quantifies precise values for the disorder on all cation symmetry sites as a function of temperature. Two samples of CZTS were fabricated by solid state reaction and their compositions were measured by inductively-coupled plasma mass ion spectroscopy, which identified significant tin loss during growth, leaving the samples Sn-poor, Cu-rich and Sn-poor, Zn-rich respectively. Both samples were found exclusively to adopt the tetragonal kesterite crystal structure with significant cation disorder, which is investigated in detail over the range 4-1275 K. Importantly, and in contrast to previous reports, the 2*a* Wyckoff site shows disorder equal to or greater than the 2*c* site. The order-disorder phase transition was observed at different temperatures for the two compositions, 489 and 501 K respectively, lower than previously reported. The kesterite-sphalerite transition was observed between 1250 and 1275 K for the Sn-poor, Cu-rich sample, significantly higher than previously reported. These results provide new insights into the high levels of disorder present in CZTS and confirm that composition and cation disorder have a significant effect on the phase transition mechanism. This work will enable the development of routes to the fabrication of higher-efficiency photovoltaic devices.

Introduction

Solar photovoltaic electricity will be an important contributor to the energy mix of the future. In 2015, it reached 229 GW peak global capacity,[1] just over 1 % of global energy demand.[2] By 2050, this is estimated to rise to 16 %.[3] However, many current materials for the absorber layer of photovoltaic solar cells, such as silicon, CdTe, and $Cu_2InGaSe_4$ (CIGS) have problems. Some are restrictively expensive, such as silicon due to high manufacturing costs and others due to element costs, particularly of Ga, In, and Te. Some contain elements not abundant enough to contribute electricity on the TW scale, such as Te, Se, and In. Some are toxic, such as Cd and Se. Many materials have a combination of these problems.[4] Lower-cost and higher-efficiency cells using Earth-abundant elements will be necessary for solar photovoltaics to achieve its potential as a major global electricity source.

Cu_2ZnSnS_4 (CZTS) is a highly promising absorber material with none of these problems. It is an intrinsically p-type direct-gap semiconductor with near-optimal band gap of 1.4-1.5 eV and high band-edge absorption coefficient $>10^4$ cm^{-1}. It currently has a best photovoltaic efficiency of 9.2 %,[5] and 12.6 % as the toxic, more expensive, and less abundant selenium-containing CZTSSe.[6] This is low compared to the records of 25.6 % for silicon,[7] 21.7 % for CIGS,[8] and 22.1 % for CdTe.[9]

Although CZTS has the potential to make a significant and sustainable contribution to global photovoltaic power generation at the TW scale, its efficiency must be approximately doubled for it to be adopted commercially. In order to do so, the low open-circuit voltage commonly reported must be increased from its current typical value of only around 60 % of the theoretical maximum.[10] Common point defects with relatively deep energy levels, such as the Cu_{Zn} and Zn_{Cu} antisites, and electrostatic potential fluctuations due to them, are likely to be limiting this.[11, 12] CZTS also has a complex phase diagram with a narrow region of stability, which is not yet fully correctly characterised, nor have the details of its crystal structure been fully resolved. Therefore a better understanding of secondary phases, defects, cation disorder within the crystal structure, and their impact on photovoltaic device performance is needed.

This work significantly improves the structural understanding of CZTS by performing high-resolution neutron powder diffraction experiments with full Rietveld refinement considering disorder on all cation lattice sites, using accurate experimentally measured compositions.

[a]Department of Physics, The University of Durham, South Road, Durham, DH1 3LE, UK
[b]Department of Earth Sciences, University College London, Gower Street, London, WC1E 6BT, UK
[c]Department of Earth Sciences, The Natural History Museum, Cromwell Road, London, SW7 5BD, UK
[d]ISIS Neutron and Muon Source, Rutherford Appleton Laboratory, Didcot, OX11 0QX, UK
*corresponding author: d.p.halliday@durham.ac.uk

CZTS Crystal Structure

CZTS has been found in several crystal structures (all illustrated in Figure 1 and described in Table 1): kesterite ($I\bar{4}$), stannite ($I\bar{4}2m$), PMCA (primitive mixed CuAu-like, $P\bar{4}2m$), and, at high temperatures, sphalerite (also called zinc blende, $F\bar{4}3m$). Additionally, a 'disordered kesterite' phase ($I\bar{4}2m$) has been observed, in which the copper and zinc atoms in the z = ¼ and ¾ planes of the kesterite structure (the 2*c* and 2*d* Wyckoff positions) are randomly distributed, with full copper occupancy remaining in the z = 0 plane (the 2*a* Wyckoff position). The kesterite and stannite structures are very similar, with the subtle difference being in the copper and zinc positions. In stannite, the zinc ions are found in the *z* = 0 and ½ plane and the copper ions in the *z* = ¼ and ¾ planes. In kesterite, the copper ions are found in the *z* = 0 and ½ plane and half of the sites in the *z* = ¼ and ¾ planes, breaking one of the mirror planes of the stannite structure.

Kesterite is the most stable structure,[13] closely followed by stannite, with enthalpies of formation -359.9 and -361.9 kJ·mol^{-1} respectively,[14] i.e. a difference of only around 3 meV per atom.[15] Hence, the structure within a sample is often not well defined, with a two-phase mixture being possible. The band gap of the stannite structure has been shown to be less than that of the kesterite,[15] so distinction between the two forms is crucial, having a major impact on photovoltaic device performance. Mixing of the kesterite and stannite phases leads to variations in the band gap of the order 100 meV,[16] which could contribute to limiting the low open-circuit voltage observed in CZTS cells, in addition to potential fluctuations caused by varying defect concentrations.

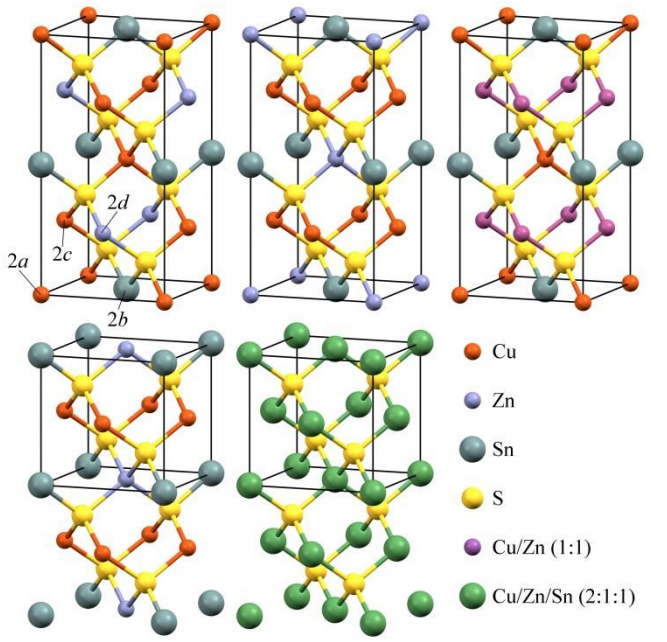

Figure 1. Possible crystal structures adopted by CZTS. Left-to-right, top: kesterite, stannite, and disordered kesterite; bottom: PMCA (primitive mixed CuAu-like) and sphalerite.

Crystal structure	Space group	Wyckoff label	Atomic position	Elements
Kesterite	$I\bar{4}$ No. 82	2*a*	(0, 0, 0)	Cu
		2*b*	(½, ½, 0)	Sn
		2*c*	(0, ½, ¼)	Cu
		2*d*	(0, ½, ¾)	Zn
		8*g*	(x, y, z)	S
Stannite	$I\bar{4}2m$ No. 121	2*a*	(0, 0, 0)	Zn
		2*b*	(½, ½, 0)	Sn
		4*d*	(0, ½, ¼)	Cu
		8*i*	(x, x, z)	S
Disordered kesterite	$I\bar{4}2m$ No. 121	2*a*	(0, 0, 0)	Cu
		2*b*	(½, ½, 0)	Sn
		4*d*	(0, ½, ¼)	Cu + Zn
		8*i*	(x, x, z)	S
PMCA	$P\bar{4}2m$ No. 111	1*a*	(0, 0, 0)	Sn
		1*d*	(½, ½, 0)	Zn
		2*f*	(0, ½, ½)	Cu
		4*n*	(x, x, z)	S
Sphalerite	$F\bar{4}3m$ No. 216	4*a*	(0, 0, 0)	Cu + Zn + Sn
		4*c*	(¼,¼,¼)	S

Table 1. Descriptions of possible CZTS crystal structures

Individual cation disorder within one of these structures is expected to be primarily only between copper and zinc, i.e. Cu_{Zn} and Zn_{Cu} antisite defects, due to the large chemical and size mismatch between tin and the other two cations. Cu_{Zn} and Zn_{Cu} point defects have been shown by ab initio calculations to have very low formation energies,[17, 18] and thus are expected to be easily formed, especially as a charge-compensated defect pair complex. This introduces antisite defect energy levels in the band gap (Cu_{Zn} at 0.15 eV above the valence band edge and Zn_{Cu} at 0.10 eV below the conduction band edge[19]), which act as recombination centres reducing device efficiency. The Cu_{Zn} defect is thought to be the cause of the p-type behaviour in most CZTS, but it is replaced as the dominant acceptor defect by the copper vacancy for Cu-poor, Zn-rich compositions, which have been found to give the best device efficiencies.[20]

Copper and zinc are isoelectronic in CZTS, so their X-ray scattering form factors, which are proportional to atomic number *Z*, are very similar. It is therefore not possible to use conventional powder X-ray diffraction (XRD) to identify the structure. This can be overcome by using the different neutron scattering lengths for copper and zinc: 7.7 and 5.7 fm respectively.[21]

Single crystal[22] and powder[23] synchrotron X-ray diffraction and neutron diffraction[24-26] have all previously been used to identify the crystal structure of CZTS and found it to be kesterite or disordered kesterite. Disorder of copper and zinc has been of particular interest; previous reports have concluded that it primarily occurs only on the Cu 2*c* and Zn 2*d* sites, and that it depends on the cooling rate after sample synthesis – 50 % antisite population at each site (i.e. complete disorder) in water-quenched samples was reduced to 30 % in

samples with a controlled cooling rate.[24] It has, however, been found that as the Cu/(Zn+Sn) ratio decreases, zinc begins to substitute for copper at the 2*a* site.[23] Copper vacancies have also been found at the 2*a* site.[27] As expected, tin has been shown to exhibit negligible disorder for stoichiometrically correct tin content.[28] The results presented here indicate that some of these findings are incorrect.

A second order phase transition to the disordered kesterite structure has been identified at 533 ± 10 K using Raman spectroscopy[16] and 552 ± 2 K using neutron diffraction,[29] and the associated expansion of the *c* lattice parameter has been observed in situ by synchrotron X-ray diffraction.[30] This implies that for usual device synthesis conditions, the disordered structure is formed, and only during a lengthy cooling process below the critical temperature can ordering occur. Thus the disorder can be controlled using the cooling process. This is supported by the observation that the Cu-Zn disorder depends on the cooling rate after sample synthesis.[24]

A further, first order, phase transition from the tetragonal disordered kesterite to the fully cation disordered cubic sphalerite structure has been reported at 1149 K, with a two-phase region between 1139 and 1156 K in which both phases exist.[30]

In addition to disorder within the CZTS phase, secondary phases are often also present in samples because the region of stability of pure CZTS in the composition phase diagram is small.[31, 32] Calculations have shown that the most common secondary phases are ZnS and Cu_2SnS_3, with CuS, SnS, SnS_2, and other ternary and quaternary secondary phases also being common. ZnS has a larger band gap than CZTS, so forms a barrier to carrier extraction, and Cu_2SnS_3 acts as a recombination centre and reduces the open-circuit voltage.[33]

Detecting ZnS and Cu_2SnS_3 using X-ray and neutron powder diffraction is difficult, and not usually possible, because the diffraction peaks overlap those of CZTS. The detection limit for using standard laboratory XRD has been estimated as 10 % for ZnS and 50 % for Cu_2SnS_3.[34]

Experimental Details

Bulk polycrystalline samples were fabricated by solid state reaction. Finely ground copper, zinc, and tin powders (of manufacturer-certified purities Cu 99.9 %, Zn 97.5 %, and Sn 99.85 %) were mixed in one alumina boat, sulphur powder (99.5 % pure, with a 30 % excess to ensure full sulphurisation) was placed in another, and both were sealed together in an evacuated quartz ampoule. The ampoules were heated with a ramping rate of 5 K·min^{-1} to 1073 K, at which they were kept for 24 hours and then left in the furnace to cool naturally back to room temperature (over ~24 hours, at a rate ~0.5 K·min^{-1}). An ampoule and sample are shown in Figure 2. For diffraction experiments the samples were ground to a fine powder using an agate mortar.

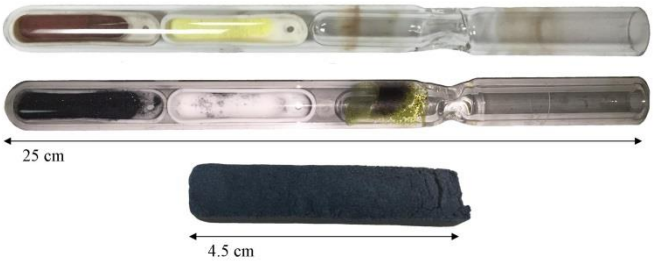

Figure 2. Top to bottom: the elemental powders sealed in an ampoule pre-heat treatment, the ampoule post-heat treatment, and the final ingot of CZTS produced.

Samples with two different starting compositions were produced: stoichiometric (B21) and Cu-poor, Zn-rich (B22), i.e. $Cu_{1.8}Zn_{1.2}SnS_4$ - optimally doped for photovoltaic application.

Inductively coupled plasma mass spectroscopy (ICPMS) was carried out using an Elan 6000 Perkin Elmer Sciex ICPMS to determine the post-fabrication elemental compositions of the samples.

SEM images, in both backscattered and secondary electron configurations, were taken using an Hitachi SU-70 FEG SEM. EDX spectroscopy was carried out using the same SEM with an INCA x-act LN2-free analytical silicon drift detector and INCA software.

Raman spectra were obtained using a Horiba JY LabRAM-HR Raman microscope system in the backscattering configuration with an LED laser to provide resonant excitation at 785 nm.

High-resolution powder neutron diffraction measurements were carried out at the HRPD beamline at ISIS. For both samples, patterns were taken at regular 10 K intervals from 4 to 480 K with the sample held in an aluminium slab can in a cryostat. Patterns were additionally taken at higher temperatures with each sample sealed in an evacuated quartz ampoule held in a vanadium can in a furnace; for sample B21, at 25 K intervals from 300 to 1275 K, and for B22, in 20 K intervals from 460 to 640 K. Patterns were taken at several temperatures in the overlapping range using both setups to ensure that the data sets are consistent with each other.

Rietveld refinement was carried out using TOPAS v4.2 & v6. Batch-processing was used to refine successively the models for the many patterns over the temperature range.

Results and Analysis

Composition

The post-fabrication compositions, measured by ICPMS for copper, zinc, and tin, and EDX for sulphur, are given in Table 2 and plotted in Figure 3. An average of 32 % of the initial tin and of 2 % of the initial zinc was lost from the samples, meaning that they became relatively much richer in copper and only slightly richer in zinc during fabrication. This is a well-known problem with CZTS fabrication due to the high vapour pressure of SnS.[35] Rather than 'stoichiometric' and 'Cu-poor, Zn-rich', the samples are better described as 'Sn-poor, Cu-rich', and 'Sn-poor, Zn-rich' respectively.

Sample	Composition	Cu	Zn	Sn	S
B21	Sn-poor, Cu-rich	28.7 %	14.4 %	9.3 %	47.6 %
B22	Sn-poor, Zn-rich	25.6 %	16.4 %	10.1 %	47.9 %

Table 2. The post-fabrication compositions measured by ICPMS.

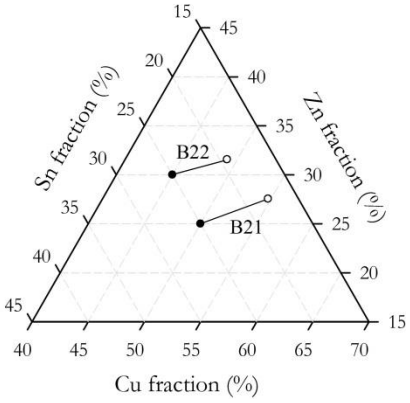

Figure 3. The starting compositions (black circles) and the final compositions measured by ICPMS (white circles) of the two samples.

SEM images of both samples are given in Figure 4, showing that they are very porous and that the Sn-poor, Cu-rich sample is very soft – so much so that it was impossible to polish a smooth surface for SEM viewing. EDX analysis, photoluminescence, and solid-state nuclear magnetic resonance (SSNMR) measurements (data not shown) all revealed no secondary phases in B21 and only negligible amounts of ZnS and SnS_2 in B22. This is confirmed by the Raman spectra shown in Figure 5, which were modelled using up to 12 peaks previously reported and identified in the literature[36-42] and are dominated by those corresponding to kesterite CZTS.

Crystal Structure

A typical neutron diffraction pattern is shown in Figure 6. Rietveld refinement shows no secondary phases are present in either sample in sufficient quantity to affect the diffraction pattern.

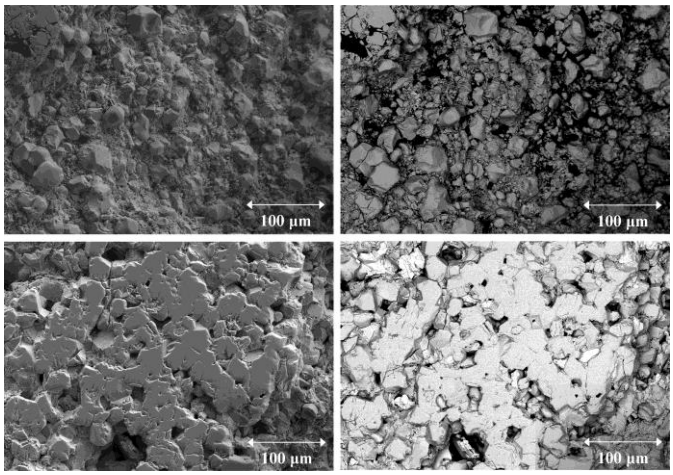

Figure 4. SEM images (left, secondary electron; and right, backscattered) of B21 (top) and B22 (bottom).

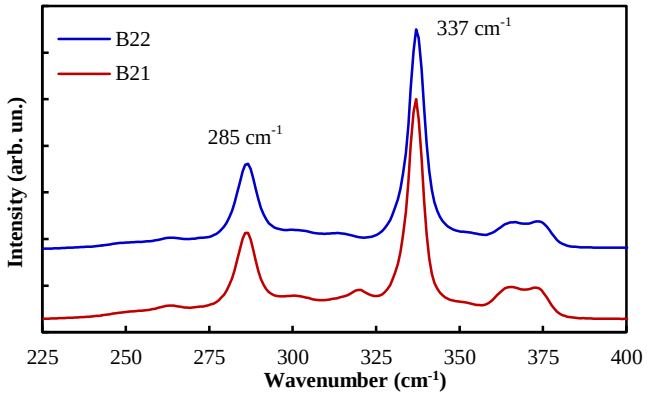

Figure 5. Raman spectra of the two samples, both dominated by the standard kesterite CZTS peaks. Labelled are the two strongest, both A modes of the kesterite structure.

It is also clear from Rietveld refinement that both samples are purely kesterite, with no stannite or PMCA phases present. PMCA gives a poor fit to the data and stannite is ruled out because although it fits the stronger peaks well, it gives a poor fit to the weaker peaks compared to kesterite.

The best model of the structure of B21, the Sn-poor, Cu-rich sample, is described in Table 3, and that for B22, the Sn-poor, Zn-rich sample, in Table 4.

Cu_{Zn} defects are dominant in B21, as expected for its Cu-rich composition, while Zn_{Cu} defects dominate in B22. This supports the theory that the better photovoltaic performance of Cu-poor devices is due to a lower concentration of Cu_{Zn} defects. Counterintuitively, there are more Zn_{Sn} than Cu_{Sn} defects in the Cu-rich B21 and vice versa for the Zn-rich B22; both give deep defect levels and are therefore detrimental to photovoltaic performance.

Temperature Variation

While sulphur and tin might be expected to be lost from the sample at high temperatures via the decomposition of CZTS into several secondary phases and the sublimation of SnS, this was not observed on sufficient a scale to affect the results. The diffraction patterns remain purely kesterite up to 1275 K, with neither SnS itself nor the phase(s) that would have been formed by the remaining elements being observed at any point.

The lattice parameter variation with temperature of both samples is plotted in Figure 7. Both compositions give approximately the same *a* values, but that *c*/2 is slightly larger below 500 K for B21, the Sn-poor, Cu-rich sample. The ratio *c*/2*a* is plotted in Figure 8, illustrating this difference between the two compositions and showing minima at the two phase transitions, which can be seen in previous data,[30] but for which no explanation has yet been proposed.

Despite almost all previous literature finding no disorder on the 2*a* site, these results show that it features Zn_{Cu} occupancy equal to the 2*c* site for Sn-poor, Cu-rich compositions, and almost as high as the 2*c* site for Sn-poor, Zn-rich compositions.

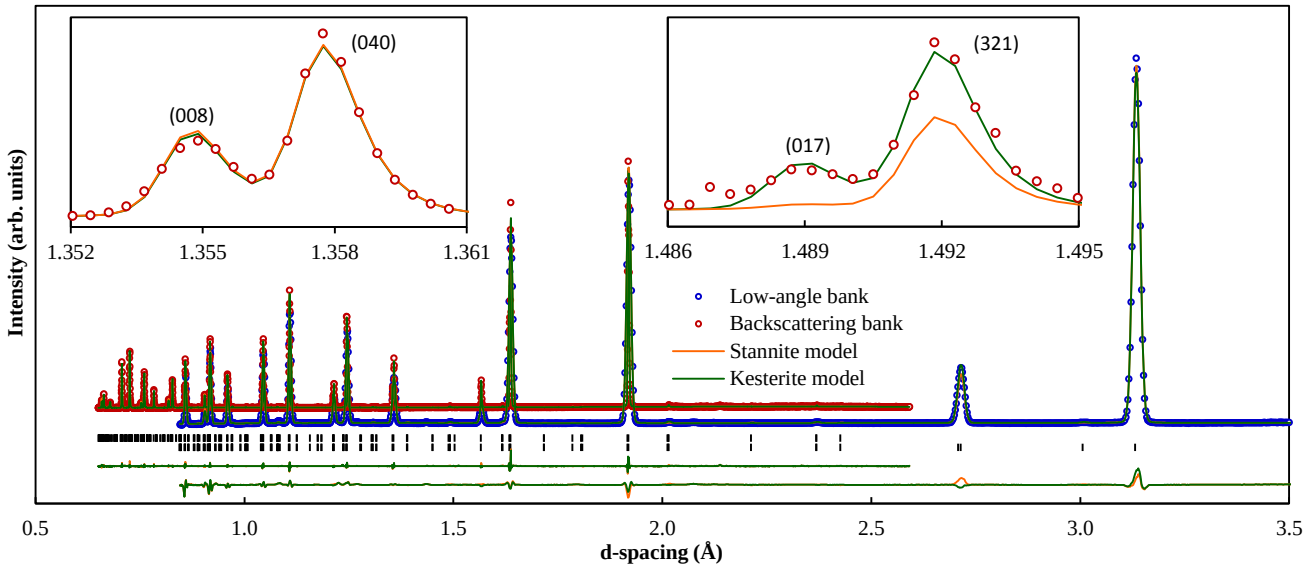

Figure 6. A neutron diffraction pattern for B21 taken at 4 K, showing data from two detector banks at HRPD, with both kesterite and stannite models plotted over the data, the peak positions marked below the patterns, and the residuals for each model for each bank at the bottom. Inset are sections of the backscattering bank pattern as examples of the tetragonal peak splitting, which demonstrate the resolution of the data; the second also shows the kesterite model fitting better than stannite.

Temperature	Lattice Parameters	Occupancies					Sulphur positions	Quality indices
		2*a* site	2*c* site	2*d* site	2*b* site	8*g* site		
4 K	***a***: 5.42321(3) Å ***c***: 10.82246(1) Å	***Cu***: 0.93(1) ***Zn***: 0.07(1)	***Cu***: 0.93(1) ***Zn***: 0.07(1)	***Cu***: 0.32(7) ***Zn***: 0.68(7)	***Cu***: 0.00(7) ***Zn***: 0.29(7) ***Sn***: 0.71(3)	***S***: 0.91(3) V_S: 0.09(3)	S_x: 0.241(2) S_y: 0.245(4) S_z: 0.128(1)	χ^2: 2.8 ***R***: 4.4
300 K	***a***: 5.43300(1) Å ***c***: 10.83527(3) Å	***Cu***: 0.96(9) ***Zn***: 0.04(9)	***Cu***: 0.86(8) ***Zn***: 0.14(8)	***Cu***: 0.37(9) ***Zn***: 0.63(9)	***Cu***: 0.00(4) ***Zn***: 0.29(4) ***Sn***: 0.71(3)	***S***: 0.91(3) V_S: 0.09(3)	S_x: 0.241(2) S_y: 0.245(4) S_z: 0.128(1)	χ^2: 2.8 ***R***: 3.6

Table 3. The best model of B21, the Sn-poor, Cu-rich sample, at 4 K and 300 K.

Temperature	Lattice Parameters	Occupancies					Sulphur positions	Quality indices
		2*a* site	2*c* site	2*d* site	2*b* site	8*g* site		
4 K	***a***: 5.42365(3) Å ***c***: 10.81813(7) Å	***Cu***: 0.74(8) ***Zn***: 0.26(8)	***Cu***: 0.90(7) ***Zn***: 0.10(7)	***Cu***: 0.10(7) ***Zn***: 0.90(7)	***Cu***: 0.22(8) ***Zn***: 0.01(8) ***Sn***: 0.77(1)	***S***: 0.92(1) V_S: 0.08(1)	S_x: 0.240(3) S_y: 0.242(5) S_z: 0.123(1)	χ^2: 3.7 ***R***: 5.2
300 K	***a***: 5.43360(1) Å ***c***: 10.83093(4) Å	***Cu***: 0.67(8) ***Zn***: 0.33(8)	***Cu***: 0.90(5) ***Zn***: 0.10(5)	***Cu***: 0.17(9) ***Zn***: 0.83(9)	***Cu***: 0.23(8) ***Zn***: 0.00(8) ***Sn***: 0.77(1)	***S***: 0.92(1) V_S: 0.08(1)	S_x: 0.240(3) S_y: 0.242(5) S_z: 0.123(1)	χ^2: 4.3 ***R***: 6.0

Table 4. The best model of B22, the Sn-poor, Zn-rich sample, at 4 K and 300 K.

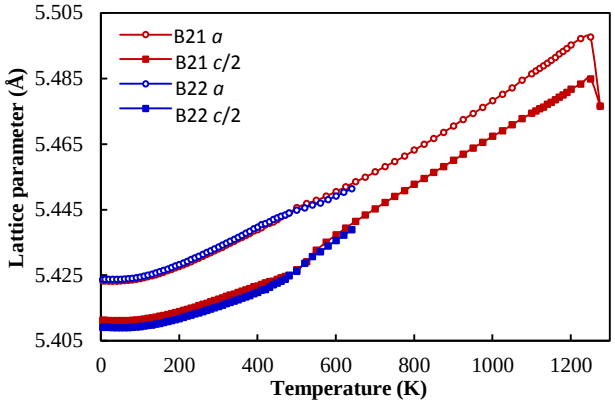

Figure 7. The lattice parameter variation with temperature of B21 (red), the Sn-poor, Cu-rich sample, and B22 (blue), the Sn-poor, Zn-rich sample, from 4 to 1275 K.

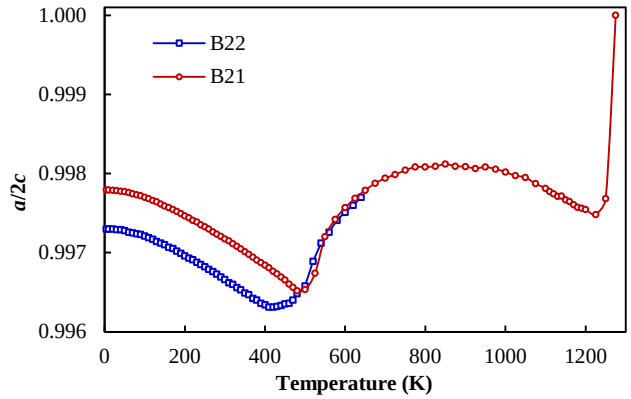

Figure 8. The ratio $c/2a$ plotted with temperature, showing minima between 400 and 500 K and at 1250 K.

Low-Temperature Thermal Expansion

Below 50 K, neither sample undergoes thermal expansion with increasing temperature, and B21 even exhibits slight negative thermal expansion of the *c* lattice parameter, shown in Figure 9. This behaviour is typical of adamantine-structured materials, many of which exhibit negative thermal expansion below 100 K, and it has previously been observed in chalcopyrite structures.[43]

Order-Disorder Phase Transition

The evolution with temperature of the copper occupancy of the 2*a*, 2*c*, and 2*d* sites is plotted in Figure 10 for both samples. Despite the large error bars, the order-disorder transition is clearly visible: the different occupancy values below around 500 K converge to within uncertainty of each other above this.

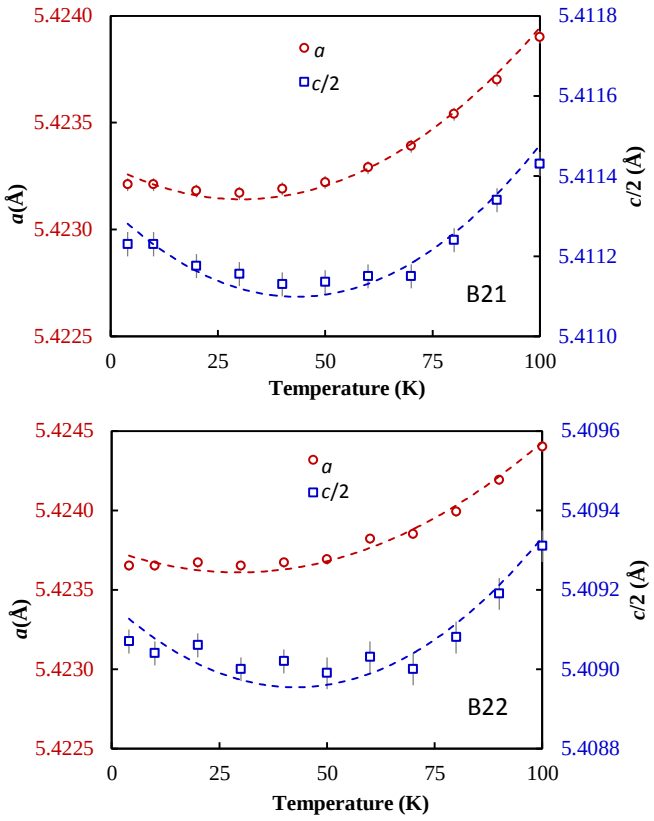

Figure 9. The low-temperature thermal expansion of the lattice parameters of, top, B21, the Sn-poor, Cu-rich sample and, bottom, B22 the Sn-poor, Zn-rich sample. The dashed lines are second order polynomial fits.

A simple model was fitted to these results, with constant occupancy values below and above the transition, the transition temperature T_C, and the full range over which it occurs w as parameters. For B21, T_C = 501 K, w = 148 K; for B22, T_C = 489 K, w = 146 K. Although the transition takes place over approximately the same temperature range for both compositions, the Sn-poor, Zn-rich composition of B22 gives a transition temperature approximately 12 K lower than the Sn-poor, Cu-rich composition of B21. The large transition range may be due simply to the equilibration and measurement time at each temperature (15 minutes and 90 minutes respectively in the relevant region) not being sufficient for the samples to reach the equilibrium state. This would artificially broaden the observed transition to higher temperatures.

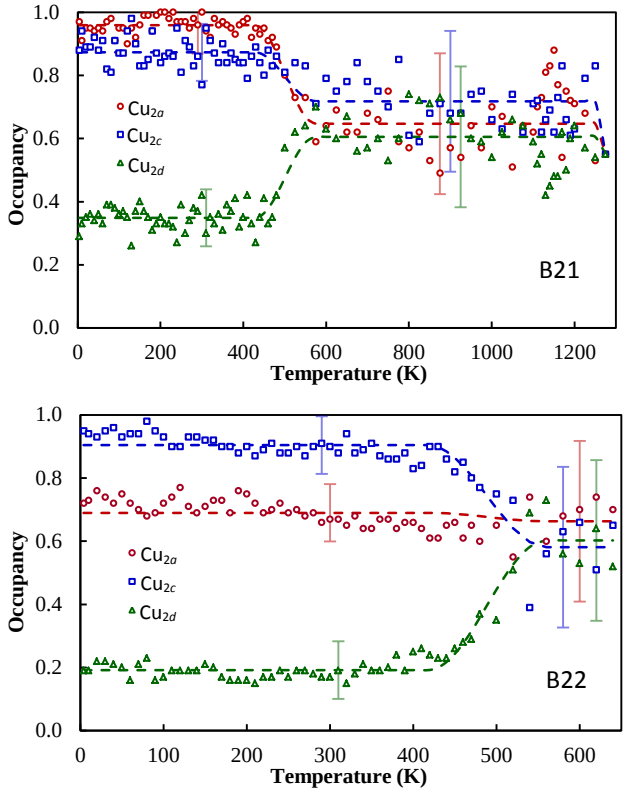

Figure 10. The evolution with temperature of the copper occupancy of the 2*a*, 2*c*, and 2*d* sites for, top, B21 the Sn-poor, Cu-rich sample and, bottom, B22 the Sn-poor, Zn-rich sample. The dashed lines are a simple model fitted to find the transition temperature and range, and the error bars are representative of the regions of data (≤480 K & ≥500 K).

For both samples, a minimum in $c/2a$ occurs in the vicinity of these temperatures, plotted in Figure 8, suggesting that this parameter is a useful indicator of the transition. The minima occur at or just below the onset of the transitions in occupancy values, suggesting that the disorder is in response to the change in lattice parameters rather than vice versa as might be expected.

The behaviour of the lattice parameters is unexplained – i.e. why the *a* lattice parameter increases at a greater rate than *c* below the transition, then *c* at a greater rate than *a* for several hundred K above the transition - but clearly the lattice parameters are significantly affected by cation disorder.

Kesterite-Sphalerite Phase Transition

The duplication at slightly different d-spacings of some peaks due to the tetragonal splitting of the kesterite structure disappears between the 1250 and 1275 K patterns, shown in Figure 11. This is indicative of the phase transition from the tetragonal kesterite structure to the cubic sphalerite.

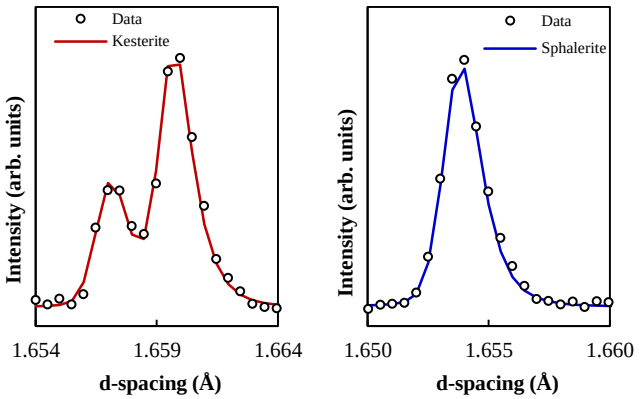

Figure 11. The (116) and (132)/(312) peaks at 1250 K (left) showing tetragonal splitting, and at 1275 K (right) showing only a single peak position, evidence of the formation of a cubic structure.

The disappearance of the tetragonal distortion is seen directly in the plot of $c/2a$ (Figure 8), which goes sharply to 1 for the 1275 K pattern. This is preceded by another local minimum in $c/2a$ at 1225 K. The plot of the lattice parameters themselves, Figure 7, shows that they not only converge in forming the cubic structure, but also decrease.

It was found that the pattern for this cubic phase at 1275 K is more accurately modelled by a sphalerite structure than simply the disordered kesterite structure with $c/2a = 1$. The difference between the sphalerite structure and the disordered kesterite is more than the lack of tetragonal distortion, but the complete mixing of all cations, including tin, equally on every cation site.

The temperature of the transition, between 1250 and 1275 K, is significantly higher than the previously reported value of between 1139 and 1156 K.[30] This suggests that this transition temperature too is very sensitive to composition.

Conclusion

Two samples of CZTS with stoichiometric (B21) and Cu-poor, Zn-rich (B22) starting compositions were fabricated by solid state reaction. Their final compositions were measured using inductively coupled plasma mass ion spectrometry and it was found that both had undergone significant tin loss during fabrication to end with Sn-poor, Cu-rich and Sn-poor, Zn-rich compositions respectively.

Their crystal structures were studied using high-resolution neutron diffraction. Both were found to adopt the kesterite crystal structure with significant cation disorder. Despite almost all previous literature finding no disorder on the 2*a* site, these results show that the 2*a* site actually features Zn_{Cu} occupancy equal to the 2*c* site for Sn-poor, Cu-rich compositions, and higher than the 2*c* site for Sn-poor, Zn-rich compositions. The resolution of this data allows the *a* and *c* lattice parameters to be reported to 6 and 7 significant figures respectively, the highest-resolution values reported to date.

Cu_{Zn} defects are dominant in B21, as expected for its Cu-rich composition, while Zn_{Cu} defects dominate in B22. This supports the theory that the better photovoltaic performance of Cu-poor devices is due to a lower concentration of Cu_{Zn} defects. Counterintuitively, there are more Zn_{Sn} than Cu_{Sn} defects in the Cu rich B21 and the opposite is true for the Zn-rich B22; both give deep defect levels and are therefore detrimental to photovoltaic performance.

Below 50 K neither sample showed positive thermal expansion, and B21 even showed slight negative expansion of the *c* lattice parameter.

An order-disorder phase transition was observed at 501 K in B21 and 489 K in B22, both lower temperatures than previously reported. It was measured to take place over a range of approximately 150 K in both samples, although this could be artificially large due to insufficient equilibration during the measurements. That the transition temperature is different for the two samples suggests that the transition mechanism is sensitive to composition. This is important to the fabrication procedure of CZTS photovoltaic cells.

A further phase transition from the tetragonal kesterite structure to the cubic sphalerite was observed in B21 between 1250 and 1275 K. This is significantly higher than previously reported, suggesting that this transition temperature is also sensitive to composition.

These findings have important consequences for the approach used to fabricate CZTS layers for optimum photovoltaic device performance. This work will enable the development of growth strategies for higher-efficiency CZTS photovoltaic devices.

The order-disorder phase transition is planned to be investigated in more detail in a future report using X-ray anomalous dispersion, and further optoelectronic study will enable the effects of crystal disorder to be quantitatively linked to material behaviour relevant to photovoltaic performance.

Acknowledgements

This work was financially supported by the UK Engineering and Physical Sciences Research Council (grant number 1335920), Diamond Light Source, and the University of Durham. Experiments at the ISIS Pulsed Neutron and Muon Source were supported by a beamtime allocation from the Science and Technology Facilities Council, and would not have been possible without the excellent technical staff there. ICPMS measurements were kindly carried out by Dr Chris Ottley and Raman facilities were provided by Prof Andrew Beeby. Thanks also go to Ruth Zhou, who assisted during some of the beamtime as part of an undergraduate project.

References

1. *Trends in Global CO_2 Emissions 2015*, EU Commission's Joint Research Centre, 2015.
2. *Key World Energy Statistics 2016*, International Energy Agency, 2016.
3. *Technology Roadmap for Solar Photovoltaic Energy 2014*, International Energy Agency, 2014.
4. A. Zuser and H. Rechberger, 'Considerations of resource availability in technology development strategies: The case study of photovoltaics'. *Resources, Conservation and Recycling*, 2011, **56**, 56-65, DOI: 10.1016/j.resconrec.2011.09.004.
5. T. Kato, H. Hiroi, N. Sakai, S. Muraoka, and H. Sugimoto, 'Characterisation of front and back interfaces on Cu_2ZnSnS_4 thin film solar cells', presented at the 27th European Photovoltaic Solar Energy Conference, Frankfurt, Germany, EU, 2012/09/25-28, 2012, DOI: 10.4229/27theupvsec2012-3co.4.2.
6. W. Wang, M. T. Winkler, O. Gunawan, T. Gokmen, T. K. Todorov, Y. Zhu, and D. B. Mitzi, 'Device characteristics of CZTSSe thin film solar cells with 12.6% efficiency'. *Advanced Energy Materials*, 2013, **4**, 1301465.1301461-1301465, DOI: 10.1002/aenm.201301465.
7. K. Masuko, M. Shigematsu, T. Hashiguchi, D. Fujishima, M. Kai, N. Yoshimura, T. Yamaguchi, Y. Ichihashi, T. Mishima, N. Matsubara, T. Yamanishi, T. Takahama, M. Taguchi, E. Maruyama, and S. Okamoto, 'Achievement of more than 25% conversion efficiency with crystalline silicon heterojunction solar cell'. *IEEE Journal of Photovoltaics*, 2014, **4**, 1433-1435, DOI: 10.1109/jphotov.2014.2352151.
8. T. M. Friedlmeier, P. Jackson, A. Bauer, D. Hariskos, O. Kiowski, R. Wuerz, and M. Powalla, 'Improved photocurrent in $Cu(In,Ga)Se_2$ solar cells: From 20.8% to 21.7% efficiency with CdS buffer and 21.0% Cd-free'. *IEEE Journal of Photovoltaics*, 2015, **5**, 1487-1491, DOI: 10.1109/jphotov.2015.2458039.
9. M. A. Green, K. Emery, Y. Hishikawa, W. Warta, E. D. Dunlop, D. H. Levi, and A. W. Y. Ho-Baillie, 'Solar cell efficiency tables (version 49)'. *Progress in Photovoltaics: Research and Applications*, 2017, **25**, 3-13, DOI: 10.1002/pip.2855.
10. X. Liu, Y. Feng, H. Cui, F. Liu, X. Hao, G. Conibeer, D. B. Mitzi, and M. Green, 'The current status and future prospects of kesterite solar cells: A brief review'. *Progress in Photovoltaics: Research and Applications*, 2016, **24**, 879-898, DOI: 10.1002/pip.2741.
11. O. Gunawan, T. Gokmen, and D. B. Mitzi, 'Suns-V_{OC} characteristics of high-performance kesterite solar cells'. *Journal of Applied Physics*, 2014, **116**, 084504.084501-084509, DOI: 10.1063/1.4893315.
12. J. J. S. Scragg, J. K. Larsen, M. Kumar, C. Persson, J. Sendler, S. Siebentritt, and C. Platzer Björkman, 'Cu–Zn disorder and band gap fluctuations in $Cu_2ZnSn(S,Se)_4$: Theoretical and experimental investigations'. *Physica Status Solidi B*, 2016, **253**, 247-254, DOI: 10.1002/pssb.201552530.
13. A. Walsh, S. Chen, S.-H. Wei, and X.-G. Gong, 'Kesterite thin film solar cells: Advances in materials modelling of Cu_2ZnSnS_4'. *Advanced Energy Materials*, 2012, **2**, 400-409, DOI: 10.1002/aenm.201100630.
14. T. Maeda, S. Nakamura, and T. Wada, 'Phase stability and electronic structure of In-free photovoltaic semiconductors, $Cu_2ZnSnSe_4$ and Cu_2ZnSnS_4 by first-principles calculation'. *MRS Proceedings*, 2009, **1165**, 137-143, DOI: 10.1557/proc-1165-m04-03.
15. S. Chen, X. G. Gong, A. Walsh, and S.-H. Wei, 'Crystal and electronic band structure of Cu_2ZnSnX_4 (X=S and Se) photovoltaic absorbers: First-principles insights'. *Applied Physics Letters*, 2009, **94**, 041903.041901-041903, DOI: 10.1063/1.3074499.
16. J. J. S. Scragg, L. Choubrac, A. Lafond, T. Ericson, and C. Platzer-Björkman, 'A low-temperature order-disorder transition in

Cu_2ZnSnS_4 thin films'. *Applied Physics Letters*, 2014, **104**, 041911.041911-041914, DOI: 10.1063/1.4863685.
17. S. Chen, J.-H. Yang, X. G. Gong, A. Walsh, and S.-H. Wei, 'Intrinsic point defects and complexes in the quaternary kesterite semiconductor Cu_2ZnSnS_4'. *Physical Review B*, 2010, **81**, 245204.245201-245210, DOI: 10.1103/physrevb.81.245204.
18. A. Nagoya, R. Asahi, R. Wahl, and G. Kresse, 'Defect formation and phase stability of Cu_2ZnSnS_4 photovoltaic material'. *Physical Review B*, 2010, **81**, 113202.113201-113204, DOI: 10.1103/physrevb.81.113202.
19. S. Chen, A. Walsh, X.-G. Gong, and S.-H. Wei, 'Classification of lattice defects in the kesterite Cu_2ZnSnS_4 and $Cu_2ZnSnSe_4$ Earth-abundant solar cell absorbers'. *Advanced Materials*, 2013, **25**, 1522-1539, DOI: 10.1002/adma.201203146.
20. S. Chen, X. G. Gong, A. Walsh, and S.-H. Wei, 'Defect physics of the kesterite thin film solar cell absorber Cu_2ZnSnS_4'. *Applied Physics Letters*, 2010, **96**, 021902.021901-021903, DOI: 10.1063/1.3275796.
21. V. F. Sears, 'Neutron scattering lengths and cross sections'. *Neutron News*, 1992, **3**, 26-37, DOI: 10.1080/10448639208218770.
22. A. Lafond, L. Choubrac, C. Guillot-Deudon, P. Fertey, M. Evain, and S. Jobic, 'X-ray resonant single-crystal diffraction technique, a powerful tool to investigate the kesterite structure of the photovoltaic Cu_2ZnSnS_4 compound'. *Acta Crystallographica B*, 2014, **70**, 390-394, DOI: 10.1107/s2052520614003138.
23. T. Washio, H. Nozaki, T. Fukano, T. Motohiro, K. Jimbo, and H. Katagiri, 'Analysis of lattice site occupancy in kesterite structure of Cu_2ZnSnS_4 films using synchrotron radiation X-ray diffraction'. *Journal of Applied Physics*, 2011, **110**, 074511.074511-074514, DOI: 10.1063/1.3642993.
24. S. Schorr, 'The crystal structure of kesterite type compounds: A neutron and X-ray diffraction study'. *Solar Energy Materials and Solar Cells*, 2011, **95**, 1482-1488, DOI: 10.1016/j.solmat.2011.01.002.
25. F. J. Espinosa-Faller, D. R. Conradson, S. C. Riha, M. B. Martucci, S. J. Fredrick, S. Vogel, A. L. Prieto, and S. D. Conradson, 'Neutron diffraction and X-ray absorption fine structure evidence for local lattice distortions and aperiodic antisite substitution in Cu_2ZnSnS_4 nanoparticles'. *The Journal of Physical Chemistry C*, 2014, **118**, 26292-26303, DOI: 10.1021/jp502150s.
26. A. Ritscher, J. Just, O. Dolotko, S. Schorr, and M. Lerch, 'A mechanochemical route to single phase Cu_2ZnSnS_4 powder'. *Journal of Alloys and Compounds*, 2016, **670**, 289-296, DOI: 10.1016/j.jallcom.2016.02.058.
27. L. Choubrac, A. Lafond, C. Guillot-Deudon, Y. Moëlo, and S. Jobic, 'Structure flexibility of the Cu_2ZnSnS_4 absorber in low-cost photovoltaic cells: From the stoichiometric to the copper-poor compounds'. *Inorganic Chemistry*, 2012, **51**, 3346-3348, DOI: 10.1021/ic202569q.
28. C. Malerba, C. L. Azanza Ricardo, M. Valentini, F. Biccari, M. Müller, L. Rebuffi, E. Esposito, P. Mangiapane, P. Scardi, and A. Mittiga, 'Stoichiometry effect on Cu_2ZnSnS_4 thin films morphological and optical properties'. *Journal of Renewable and Sustainable Energy*, 2014, **6**, 011404.011401-011412, DOI: 10.1063/1.4866258.
29. A. Ritscher, M. Hoelzel, and M. Lerch, 'The order-disorder transition in Cu_2ZnSnS_4 – A neutron scattering investigation'. *Journal of Solid State Chemistry*, 2016, **238**, 68-73, DOI: 10.1016/j.jssc.2016.03.013.
30. S. Schorr and G. Gonzalez-Aviles, 'In-situ investigation of the structural phase transition in kesterite'. *Physica Status Solidi A*, 2009, **206**, 1054-1058, DOI: 10.1002/pssa.200881214.
31. I. D. Olekseyuk, I. V. Dudchak, and L. V. Piskach, 'Phase equilibria in the Cu_2S-ZnS-SnS_2 system'. *Journal of Alloys and Compounds*, 2004, **368**, 135-143, DOI: 10.1016/j.jallcom.2003.08.084.
32. J. Scragg, PhD, University of Bath, 2010.
33. M. Kumar, A. Dubey, N. Adhikari, S. Venkatesan, and Q. Qiao, 'Strategic review of secondary phases, defects and defect-complexes in kesterite CZTS-Se solar cells'. *Energy & Environmental Science*, 2015, **8**, 3134-3159, DOI: 10.1039/c5ee02153g.
34. D. M. Berg, M. Arasimowicz, R. Djemour, L. Gütay, S. Siebentritt, S. Schorr, X. Fontané, V. Izquierdo-Roca, A. Pérez-Rodriguez, and P. J. Dale, 'Discrimination and detection limits of secondary phases in Cu_2ZnSnS_4 using X-ray diffraction and Raman spectroscopy'. *Thin Solid Films*, 2014, **569**, 113-123, DOI: 10.1016/j.tsf.2014.08.028.
35. V. Piacente, S. Foglia, and P. Scardala, 'Sublimation study of the tin sulphides SnS_2, Sn_2S_3 and SnS'. *Journal of Alloys and Compounds*, 1991, **177**, 17-30, DOI: 10.1016/0925-8388(91)90053-x.
36. Y. C. Cheng, C. Q. Jin, F. Gao, X. L. Wu, W. Zhong, S. H. Li, and P. K. Chu, 'Raman scattering study of zinc blende and wurtzite ZnS'. *Journal of Applied Physics*, 2009, **106**, 123505.123501-123505, DOI: 10.1063/1.3270401.
37. P. A. Fernandes, P. M. P. Salomé, and A. F. da Cunha, 'Study of polycrystalline Cu_2ZnSnS_4 films by Raman scattering'. *Journal of Alloys and Compounds*, 2011, **509**, 7600-7606, DOI: 10.1016/j.jallcom.2011.04.097.
38. T. Gürel, C. Sevik, and T. Çağın, 'Characterisation of vibrational and mechanical properties of quaternary compounds Cu_2ZnSnS_4 and $Cu_2ZnSnSe_4$ in kesterite and stannite structures'. *Physical Review B*, 2011, **84**, 205201.205201-205207, DOI: 10.1103/physrevb.84.205201.
39. A. Khare, B. Himmetoglu, M. Johnson, D. J. Norris, M. Cococcioni, and E. S. Aydil, 'Calculation of the lattice dynamics and Raman spectra of copper zinc tin chalcogenides and comparison to experiments'. *Journal of Applied Physics*, 2012, **111**, 083707.083701-083709, DOI: 10.1063/1.4704191.
40. D. Dumcenco and Y.-S. Huang, 'The vibrational properties study of kesterite Cu_2ZnSnS_4 single crystals by using polarisation dependent Raman spectroscopy'. *Optical Materials*, 2013, **35**, 419-425, DOI: 10.1016/j.optmat.2012.09.031.
41. M. Dimitrievska, A. Fairbrother, A. Pérez-Rodríguez, E. Saucedo, and V. Izquierdo-Roca, 'Raman scattering crystalline assessment of polycrystalline Cu_2ZnSnS_4 thin films for sustainable photovoltaic technologies: Phonon confinement model'. *Acta Materialia*, 2014, **70**, 272-280, DOI: 10.1016/j.actamat.2014.02.035.
42. M. Guc, S. Levcenko, I. V. Bodnar, V. Izquierdo-Roca, X. Fontane, L. V. Volkova, E. Arushanov, and A. Pérez-Rodríguez, 'Polarised Raman scattering study of kesterite type Cu_2ZnSnS_4 single crystals'. *Scientific Reports*, 2016, **6**, 19414.19411-19417, DOI: 10.1038/srep19414.
43. K. S. Knight, W. G. Marshall, and S. W. Zochowski, 'The low-temperature and high-pressure thermoelastic and structural properties of chalcopyrite $CuFeS_2$'. *The Canadian Mineralogist*, 2011, **49**, 1015-1034, DOI: 10.3749/canmin.49.4.1015.